# Simplified channel model for indoor VLC systems

QIONG ZHAO, WEILIN ZHANG, CHEN CHEN, 2,\* D AND BO BAI DO BAI

**Abstract:** The channel model of indoor visible light communication (VLC) is primarily influenced by the receiver's position and orientation. In this study, we decouple the effects of receiver position and orientation, treating them as independent random variables. This decoupling enables a clearer understanding of how each factor independently influences the channel model. Specifically, we focus on the impact of the azimuth angle, a critical component of orientation, on the VLC channel. We present a simplified channel model for indoor VLC systems based on partial orientation information. Theoretical analysis and simulation results collectively indicate that the accuracy of the simplified channel model is influenced by the field-of-view (FOV), with higher accuracy achieved at narrower FOVs. To evaluate practical performance, we compare our simplified model with the existing complete channel model in a two-user precoding system. Results show that our proposed simplified channel model maintains value, particularly in narrow-FOV scenarios. The research findings indicate that this simplified model is suitable for applications with high demands for channel accuracy in narrow-FOV indoor VLC systems, and can be extended to applications in wide-FOV systems where perfect channel information is not required.

© 2024 Optica Publishing Group under the terms of the Optica Open Access Publishing Agreement

#### 1. Introduction

Indoor visible light communication (VLC) has emerged as a promising short-distance transmission technology, garnering increasing attention [1–4]. In indoor VLC systems, light signals are transmitted and received by light-emitting diodes (LEDs) and photo-diodes (PDs), respectively. Different from radio frequency (RF) channels, whose variations are governed by doppler and multipath effects, indoor VLC channel variations are mainly related to PD position and orientation, where the line-of-sight (LOS) component is dominant compared to the reflection components. Owing to these unique transmission mechanisms, the channel model of indoor VLC systems is markedly different from that of RF communication systems [5–7].

As a basic researching field of wireless communication technologies, channel modeling significantly serves to the system design and optimization [8]. The direct current (DC) gain of the infrared channel's LOS component was described in [9] and has been widely applied in indoor VLC systems. In early studies, researchers usually assumed that the orientation of a PD is constant over time [10]. However, people tend to use their smart-phones in comfortable manners, which means that the PD of a smart-phone always has a random and time-variant orientation. With the rapid deployment of mobile devices, more and more researches begin to focus on the variation of the VLC channel state with a random PD orientation [11–14].

The authors in [11] investigated the effect of a PD's random orientation on the LOS channel gain to simulate a randomly placed mobile device. They developed an analytical framework to characterize the statistical distribution of the LOS channel gain. Furthermore, the authors in

#527917 Journal © 2024 https://doi.org/10.1364/OE.527917

<sup>&</sup>lt;sup>1</sup>School of Communications and Information Engineering, Xi'an University of Posts & Telecommunications, Xi'an, Shaanxi 710121, China

 $<sup>^2</sup>$ School of Microelectronics and Communication Engineering, Chongqing University, Chongqing 401331, China

<sup>&</sup>lt;sup>3</sup> School of Telecommunications Engineering, Xidian University, Xi'an, Shaanxi 710071, China \*c.chen@cqu.edu.cn

[12] modeled the orientation of a PD. The receiving PD's orientation was represented by the polar angle and the azimuthal angle. They presented the probability density function (PDF) of the polar angle, which laid the foundation for the research of LOS channel gain with random PD orientations. Moreover, the series-form expressions for the statistics of the VLC channel by considering random wide field-of-view (FOV) orientation and location of the receiver have been studied in [15]. These researches are useful to reveal the impact of receiver position and orientation on the VLC channel as well as optimize the system design.

However, prior research on orientation has typically approached the subject in one of two ways: either by considering orientation in its entirety or by concentrating on the polar angle alone. Azimuthal angle is another important part of PD orientation, which receives insufficient attention. The authors in [13] had pointed out that the LOS channel gain was fairly tolerant to the changes of the azimuthal angle, but the analytical expression for the effect of the azimuthal angle on the LOS channel gain was not derived in the literature. What is more, the azimuthal angle of the receiving PD is more volatile than the polar angle in actual scenarios, which makes it difficult to obtain its accurate value.

In this paper, we investigate the effects of the azimuthal angle on VLC channel, propose a simplified channel model, and evaluated the accuracy of the model as well as its performance in practical applications. The main contributions of this paper are summarized as follows

- 1. An analytical expression of the LOS channel for the VLC link is derived, which is a function of the receiving PD's position and orientation.
- 2. The effect of the PD azimuthal angle on the LOS channel is evaluated by both theoretical analysis and simulation verification.
- 3. A simplified channel model is introduced, followed by an assessment of its accuracy across various system configurations.
- 4. The performance assessment of the proposed simplified channel model in two-user precoding indoor VLC system is conducted to evaluate its practicality.

The remainder of this paper is organized as follows. In Section 2, we decompose the influence of the PD position and orientation to derive an analytical expression for the LOS channel in the VLC link. In Section 3, we analysis the effects of the azimuthal angle on indoor VLC channel. We then introduce the architecture of our proposed channel model and analyze its reliability in Section 4, followed by the performance evaluation of the simplified channel model in Section 5. Finally, we draw the conclusions of our work in Section 6.

# 2. System model

We consider the LOS link in the VLC downlink, as shown in Fig. 1, where the LED on the ceiling is the transmitter and the PD carried by the user is the receiver. According to the Lambertian radiation model [9], the channel gain of the LOS link can be modeled as:

$$h = \frac{(m+1)A}{2\pi d^2} \cos^m(\phi) \cos(\varphi), (\varphi \le \Psi_c)$$
 (1)

Here, the parameter  $m=-\log(2)/\log(\cos(\Phi_{1/2}))$  signifies the order of the Lambertian emission, where  $\Phi_{1/2}$  represents the semi-angle of the LED. Additionally, A denotes the geometric area of the PD and d corresponds to the Euclidean distance between the ceiling and the receiving plane. The term  $\Psi_c$  represents the receiver FOV, with  $\phi$  being the irradiance angle and  $\varphi$  denoting the incidence angle.

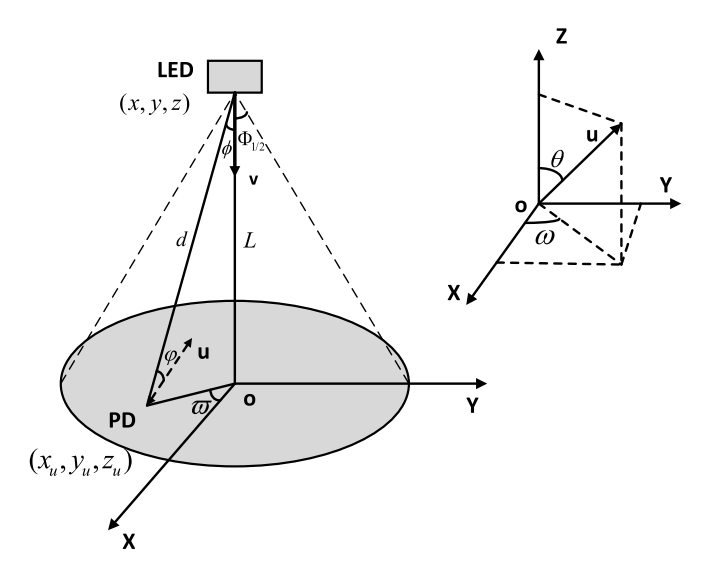


Fig. 1. The point-to-point VLC downlink system model.

Taking  $d = L/\cos(\phi)$  into Eq. (1), we can get another expression of Eq. (1) as:

$$h = \frac{(m+1)A}{2\pi L^2} \cos^{(m+2)}(\phi) \cos(\varphi), (\varphi \le \Psi_c)$$
 (2)

where L is the vertical distance between the ceiling and the receiving plane.

Since the LED is usually fixed vertically downward to the ceiling in indoor scenes, we assume that it has a fixed position (x, y, z) in the geographic coordinate system. Using indoor positioning methods [10,16], we can also determine a PD's position  $(x_u, y_u, z_u)$  in the room. Obviously, the incidence angle  $\varphi$  is depended on the orientation of the PD and the relative position of the LED and the PD. The orientation of the PD which is denoted as  $(\theta, \omega)$  in the Geographic coordinate system can be determined by the output of the inertial measurement unit configured in the user terminal [12], where  $\theta$  is the polar angle and  $\omega$  is the azimuth angle as shown in the subset of Fig. 1. We transform Eq. (14) from Ref. [12] to derive a new expression of  $\cos(\varphi)$  as:

$$\cos(\varphi) = \frac{\Delta x \sin(\theta) \cos(\omega) + \Delta y \sin(\theta) \sin(\omega) + \Delta z \cos(\theta)}{d}$$
(3)

where  $d = \sqrt{(x - x_u)^2 + (y - y_u)^2 + (z - z_u)^2}$ ,  $\Delta x = x - x_u$ ,  $\Delta y = y - y_u$ , and  $\Delta z = z - z_u$ . We can see form Eq. (3) that the influence of position and orientation on the channel is intertwined through  $\cos(\varphi)$ .

To achieve the separation of positional and orientational influences, it is essential to reconfigure the expressions related to  $\cos(\varphi)$ . Referring to the definition of orientation, we employ polar coordinate parameters to represent the position as  $(\phi, \varpi)$ , where  $\varpi$  is the angle between the projection of the line connecting the LED and the PD in the given receiver plane, and the positive direction of the X-axis in the Geographic coordinate system. In this paper, we designate  $\phi$  as the position-related polarization angle and  $\varpi$  as the position-related azimuth angle. It is important to note that  $\phi$  and  $\varpi$  are two independent random variables.

According to the geometry relationship exhibited in Fig. 1, we can get:

$$\begin{cases} \frac{\Delta x}{d} = -\cos(\varpi)\sin(\phi) \\ \frac{\Delta y}{d} = -\sin(\varpi)\sin(\phi) \\ \frac{\Delta z}{d} = \cos(\phi) \end{cases}$$
 (4)

Substituting Eq. (4) into Eq. (3), we can get:

$$\cos(\varphi) = \underbrace{\cos(\phi)}_{\text{position orientation}} \underbrace{\cos(\theta)}_{\text{position orientation}} - \underbrace{\sin(\phi)}_{\text{position orientation}} \underbrace{\sin(\theta)}_{\text{position orientation}} \underbrace{\cos(\omega)}_{\text{position orientation}} + \underbrace{\sin(\omega)}_{\text{position orientation}}$$
(5)

We can see from Eq. (5) that the cosine of the incidence angle is a complex parameter that is related to both the position and the orientation. Since  $\theta$  and  $\omega$  are mutually independent and they are both azimuth angle-related variables, we make  $\delta_{\omega} = \varpi - \omega$ , where  $\delta_{\omega}$  can be taken as a azimuth angle-related variable. Therefore, The expression of  $\cos(\varphi)$  can be simplified as:

$$\cos(\varphi) = \cos(\phi)\cos(\theta) - \sin(\phi)\sin(\theta)\cos(\delta_{\omega}) \tag{6}$$

Then we can represent the channel gain of the LOS link as:

$$h = \frac{(m+1)A}{2\pi L^2} \cos^{(m+2)}(\phi) [\cos(\phi)\cos(\theta) - \sin(\phi)\sin(\theta)\cos(\delta_{\omega})]$$
 (7)

Considerable research attention has been devoted to studying the influence of parameters such as L,  $\phi$ , and  $\theta$  on the channel gain of the LOS link, yielding valuable insights for analyzing the characteristics of indoor VLC channels [17–20]. However, the investigation into the impact of the azimuth angle on the channel gain of the LOS link remains inadequate, lacking a comprehensive analysis.

#### 3. Effects of azimuthal angle on indoor VLC channel

The influence of azimuth angle on the indoor VLC channel is manifested through its modulation of  $\cos(\varphi)$ , subsequently influencing the channel gain of the LOS link. Accordingly, our analysis initiates by evaluating the effects of  $\varpi$  and  $\omega$  on  $\cos(\varphi)$ , followed by the application of these insights to the channel gain of the LOS link.

Preliminary studies have shown that  $\varpi$  and  $\omega$  can be modeled as uniformly distributed random variables, which can be described as  $\varpi \sim \mathcal{U}[0,2\pi]$  and  $\omega \sim \mathcal{U}[0,2\pi]$  [12]. Given that  $\varpi$  and  $\omega$  are independent random variables,  $\delta_{\omega} = \varpi - \omega$  constitutes a random variable with its own PDF as:

$$f(\delta_{\omega}) = \frac{2\pi - |\delta_{\omega}|}{4\pi^2}, \quad -2\pi \le \delta_{\omega} \le 2\pi, \tag{8}$$

Furthermore, defining  $u = \cos(\delta_{\omega})$ , the PDF of u can be expressed as:

$$f(u) = \frac{1}{\pi\sqrt{1 - u^2}}, -1 < u < 1 \tag{9}$$

Consequently, the constraint condition  $\varphi \leq \Psi_c$  given in Eq. (2) can be expressed as:

$$\cos(\Psi_c) \le \cos(\phi)\cos(\theta) - \sin(\phi)\sin(\theta)\cos(\delta_{\omega}) = \cos(\phi) \tag{10}$$

Modifying, we can get:

$$u = \cos(\delta_{\omega}) \le \frac{\cos(\phi)\cos(\theta) - \cos(\Psi_c)}{\sin(\phi)\sin(\theta)}$$
 (11)

Defining  $b = min(\frac{\cos(\phi)\cos(\theta) - \cos(\Psi_c)}{\sin(\phi)\sin(\theta)}, 1)$  and considering  $\cos(\delta_\omega)$  is subject to the constraint  $-1 \le \cos(\delta_\omega) \le 1$ , we can get:

$$-1 \le u \le b \tag{12}$$

In the event that u is erroneously estimated as  $\hat{u}$ , the discrepancy in the cosin of the incidence angle be gauged by the mean square error (MSE):

$$MSE = E[(\cos(\varphi) - \cos(\hat{\varphi}))^2] = E[(u - \hat{u})^2 \sin^2(\phi) \sin^2(\theta)]$$
(13)

For a fixed set of  $\phi$  and  $\theta$ , the precision of  $\cos(\varphi)$ , taking into account the complete range of u values, Eq. (13) can be expressed as:

$$MSE = \frac{\int_{-1}^{b} (u - \hat{u})^2 \sin^2(\phi) \sin^2(\theta) f(u) du}{\int_{-1}^{b} f(u) du}$$
(14)

Equation (14) elucidates the influence of  $\phi$  and  $\theta$  on the MSE of  $\cos(\varphi)$ . Expanding upon this, our analysis will now delve into the effect of  $\cos(\delta_{\omega})$  on the MSE of  $\cos(\varphi)$ , considering the potential range of values for  $\phi$  and  $\theta$ . Since  $-1 \le \cos(\delta_{\omega}) \le b$  and  $b \le 1$  we can get:

$$\cos(\phi)\cos(\theta) - \sin(\phi)\sin(\theta) \le \cos(\phi) \le \cos(\phi)\cos(\theta) + \sin(\phi)\sin(\theta) \tag{15}$$

Taking  $\cos(\phi + \theta) = \cos(\phi)\cos(\theta) - \sin(\phi)\sin(\theta)$  and  $\cos(\phi - \theta) = \cos(\phi)\cos(\theta) + \sin(\phi)\sin(\theta)$  into Eq. (15), we can get:

$$\cos(\phi + \theta) \le \cos(\varphi) \le \cos(\phi - \theta) \tag{16}$$

To simultaneously satisfy the constraints provided by Eq. (15) and Eq. (16), we provide the following constraints:

$$\begin{cases}
\cos(\phi + \theta) \ge \cos(\Psi_c) \\
\cos(\phi + \theta) \le \cos(\Psi_c), \quad \cos(\phi - \theta) \ge \cos(\Psi_c)
\end{cases}$$
(17)

Then the potential range of values for  $\phi$  and  $\theta$  that satisfies constraint condition outlined in Eq. (10) can be transformed as:

$$\begin{cases}
\mathbf{Case1} : & \phi + \theta \le \Psi_c \\
\mathbf{Case2} : & \Psi_c < \phi + \theta, \quad |\phi - \theta| < \Psi_c
\end{cases}$$
(18)

Subsequently, we assess the impact of  $\cos(\delta_{\omega})$  on the average error of  $\cos(\varphi)$  within the entire possible range of  $\phi$  and  $\theta$ .

For **case 1**, we can derive that  $\frac{\cos(\phi)\cos(\theta)-\cos(\Psi_c)}{\sin(\phi)\sin(\theta)} \ge 1$ , then b=1 and  $\int_{-1}^b f(u)du=1$ . Substituting Eq. (9) into Eq. (14), we can get:

$$MSE = \sin^2(\phi)\sin^2(\theta)(\frac{1}{2} + \hat{\mu}^2)$$
 (19)

By applying the minimum mean square error (MMSE) criterion, we can derive the optimal  $\hat{u}$  by differentiating the MSE with respect to  $\hat{u}$  and setting  $\frac{\partial MSE}{\partial \hat{u}} = 0$ . After differentiating and simplifying, we obtain the optimal  $\hat{u}$  as  $\hat{u} = 0$ . Substituting  $\hat{u} = 0$  into Eq. (19), we get the MSE

of  $cos(\varphi)$  as:

$$MSE \stackrel{\hat{u}=0}{=} \frac{1}{2} \sin^2(\phi) \sin^2(\theta) \tag{20}$$

From Eq. (20), we can see that MSE increases with  $\phi$  and  $\theta$ . Since  $\phi + \theta \le \Psi_c$ , we can obtain the maximum of MSE as:

$$MSE_{\text{max}} \stackrel{\phi = \theta = \frac{\Psi_c}{2}}{=} \frac{1}{2} \sin^4(\frac{\Psi_c}{2}) \tag{21}$$

For **case 2**, we can derive that  $\frac{\cos(\phi)\cos(\theta)-\cos(\Psi_c)}{\sin(\phi)\sin(\theta)} \le 1$ , then  $b = \frac{\cos(\phi)\cos(\theta)-\cos(\Psi_c)}{\sin(\phi)\sin(\theta)}$  and  $\int_{-1}^b f(u)du = \frac{\pi+2\arcsin(b)}{2\pi}$ . Next, we try to solve Eq. (14) based on the value of  $\hat{u}$ . Substituting Eq. (9) into Eq. (14), we can get:

$$MSE = \sin^2(\phi)\sin^2(\theta)\left[\frac{\sqrt{1 - b^2}(4\hat{u} - b)}{\pi + 2\arcsin(b)} + \hat{u}^2 + \frac{1}{2}\right]$$
 (22)

By applying the MMSE criterion, we can derive the optimal  $\hat{u}$  by differentiating the MSE with respect to  $\hat{u}$  and setting  $\frac{\partial MSE}{\partial \hat{u}} = 0$ . After differentiating and simplifying, we obtain the optimal  $\hat{u}$  as  $\hat{u} = -\frac{2\sqrt{1-b^2}}{\pi+2\arcsin(b)}$ . Substituting  $\hat{u} = -\frac{2\sqrt{1-b^2}}{\pi+2\arcsin(b)}$  into Eq. (22), we get the MSE of  $cos(\varphi)$  as:

$$MSE = \frac{\hat{u} = -\frac{2\sqrt{1-b^2}}{\pi + 2\arcsin(b)}}{\sin^2(\phi)\sin^2(\theta)(\frac{1}{2} - \frac{4(1-b^2)}{(\pi + 2\arcsin(b))^2} - \frac{b\sqrt{1-b^2}}{\pi + 2\arcsin(b)})$$
(23)

From Eq. (23), we can see that the MSE increases with  $\phi$  and  $\theta$ . Since  $\Psi_c < \phi + \theta < 2\pi - \Psi_c$  and  $|\phi - \theta| < \Psi_c$ , we can obtain the maximum of MSE as:

$$MSE_{\text{max}} \stackrel{\phi = \theta = \pi - \frac{\Psi_c}{2}}{====} \frac{1}{2} \sin^4(\frac{\Psi_c}{2})$$
 (24)

Equations (21) and (24) indicate the maximum MSE associated with substituting a fixed orientation angle for the true orientation angle in  $\cos(\varphi)$  is independent of parameters  $\phi$  and  $\theta$ , and is solely related to the FOV. Moreover, the larger the FOV angle, the greater the corresponding MSE

To more clearly illustrate this pattern, Fig. 2 depicts the curve of maximum error values for different FOVs. We can see that both the maximum MSE and its growth rate increase with the

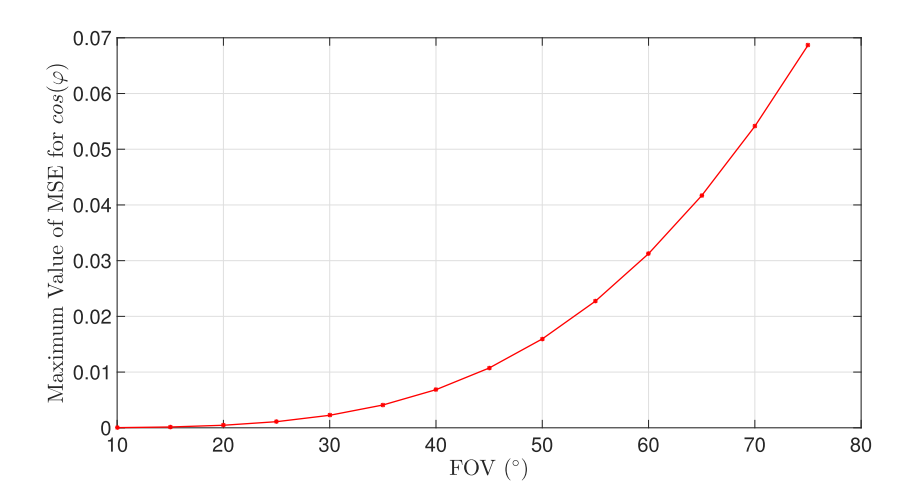
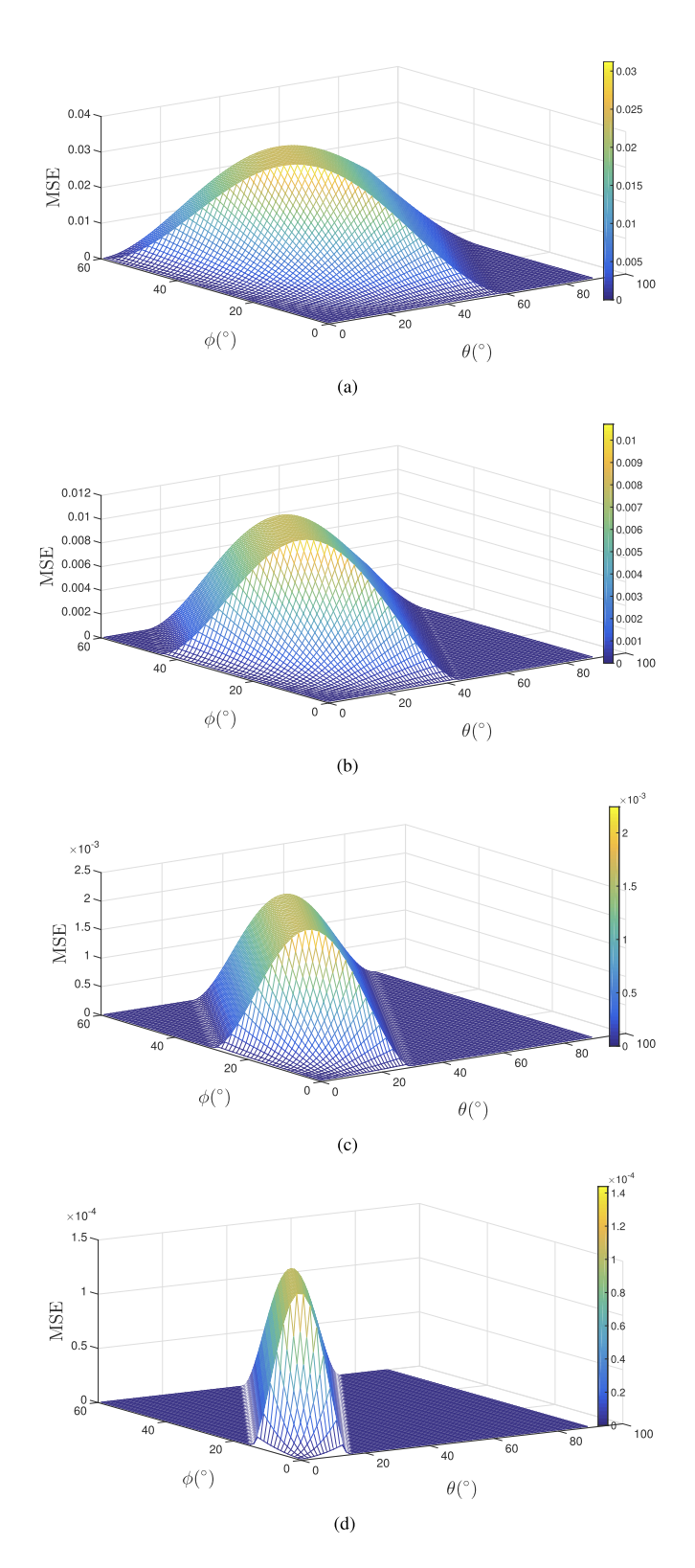


Fig. 2. The maximum value of MSE under different FOV settings.



**Fig. 3.** The distribution of MSE. (a) FOV= $60^{\circ}$ . (b) FOV= $45^{\circ}$ . (c) FOV= $30^{\circ}$ . (d) FOV= $15^{\circ}$ .

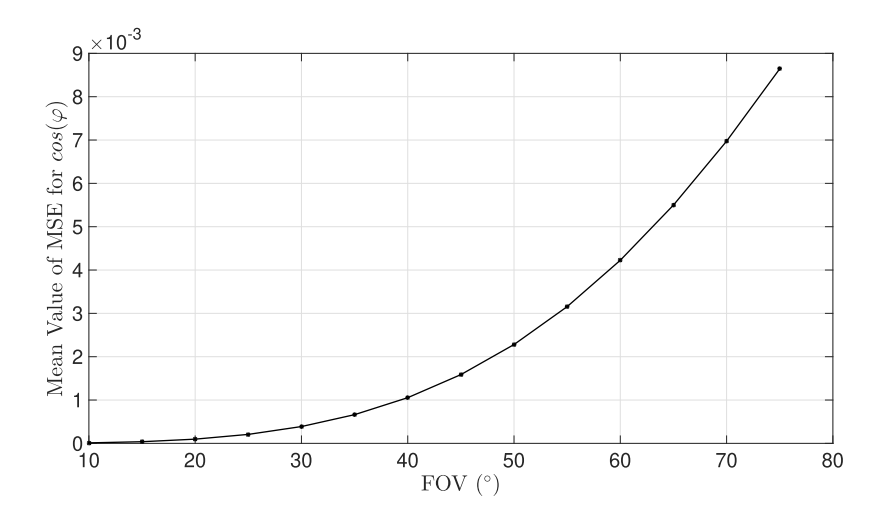


Fig. 4. The mean value of MSE under different FOV settings.

enlargement of the FOV. When the FOV is less than 40°, the maximum value of the MSE is below 0.1. To analyze the distribution of MSE across the entire range of possible values for parameters  $\phi$  and  $\theta$ , we conduct a simulation to examine the distribution of the MSE of  $\cos(\varphi)$  under the condition of  $\hat{u}=0$  for Case 1 and  $\hat{u}=-\frac{2\sqrt{1-b^2}}{\pi+2\arcsin(b)}$  for Case 2.

In simulation, we assume the LED is positioned vertically to the horizontal plane, with a

In simulation, we assume the LED is positioned vertically to the horizontal plane, with a half-power beam width of  $\Phi_{1/2} = 60^{\circ}$ , and the receiving area A of the PD is  $1 \text{cm}^2$ . We traverse  $\theta$  and  $\phi$  within the ranges of  $[0^{\circ}, 90^{\circ}]$  and  $[0^{\circ}, 60^{\circ}]$  respectively, both with an interval of  $1^{\circ}$  under the prescribed FOV. For each trial, the conditions are first evaluated to determine which of the two criteria, **case 1** or **case 2**, is satisfied based on the values of parameters  $\phi$  and  $\theta$ . Subsequently, the value of  $\hat{u}$  is selected based on the evaluation results. Finally,  $\cos(\hat{\varphi})$  at a given  $\hat{u}$  is computed. Concurrently, for each trial, we traverse  $\delta_{\omega}$  values  $0^{\circ}$  to  $360^{\circ}$  at intervals of  $1^{\circ}$  and calculate the squared difference between the  $\cos(\varphi)$  values and  $\cos(\hat{\varphi})$  for each specific  $\delta_{\omega}$ . We then calculate the mean of these squared differences across all  $\cos(\hat{\varphi})$  samples, which serves as the MSE for this trial. The simulation results are presents in Fig. 3. Limited by manuscript length, we confine our results to four specific FOVs.

Figure 3 illustrates that MSE of  $\cos(\varphi)$  for a specified set of parameters  $\phi$  and  $\theta$  is reduced as the FOV decreases. This reduction is due to the fact that a narrower FOV angle confines the effective receiving area of the receiver, thereby narrowing the permissible range for the parameters  $\phi$  and  $\theta$ . Consequently, as the FOV decreases, the potential values and upper bounds  $\phi$  and  $\theta$  are also constrained to a smaller range. These simulation results are consistent with the formulations presented in Eq. (21) and Eq. (24).

To further illustrate the impact of the FOV on the MSE of  $\cos(\varphi)$ , Fig. 4 presents the curves showing the mean values of MSE as the FOV varies. We can see that the average value of MSE is lower than 0.001 when the FOV is less than 40°. Even at a FOV of 70°, the average value of MSE does not exceed the 0.007. Consequently, we can conclude that maintaining  $\cos(\delta_{\omega})$  at specific fixed values has a limited impact on the accuracy of  $\cos(\varphi)$ .

#### 4. Simplified LOS channel model for indoor VLC system

## 4.1. Detailed presentation of the simplified channel model

Given the minimal impact of the azimuthal angle on the accuracy of  $\cos(\varphi)$ , we extend this observation to the LOS channel gain. Consequently, we infer that maintaining  $\cos(\delta_{\omega})$  at specific

fixed values has limited influence on the accuracy of modeling the LOS channel gain, especially in scenarios characterized by a narrow FOV. Therefore, we choose to disregard these minor factors and propose a simplified LOS channel model for indoor VLC systems as:

$$h = \frac{(m+1)A}{2\pi L^2} \cos^{(m+2)}(\phi) [\cos(\phi)\cos(\theta) - \hat{u}\sin(\phi)\sin(\theta)]$$
 (25)

where  $\hat{u}=0$  for the case  $\phi+\theta\leq\Psi_c$ , and  $\hat{u}=-\frac{2\sqrt{1-b^2}}{\pi+2\arcsin(b)}$  for the case  $\Phi\leq\phi+\theta\leq2\pi-\Psi_c, |\phi-\theta|<\Psi_c$ .

## 4.2. Accuracy of the simplified channel model

To more intuitively demonstrate the error of the simplified channel model compared to the existing complete channel model, we introduce the relative mean square error (RMSE) as an observation metric to measure the differences between them. The definition of the RMSE is as follows.

$$RMSE = \frac{1}{N} \sum \frac{(\hat{h} - h)^2}{h^2}$$
 (26)

where N is the number of random samples, h and  $\hat{h}$  are the LOS channel gains defined by Eq. (1) and Eq. (25), respectively. The RMSE serves as an indicator of the fidelity with which the simplified channel model approximates the existing complete channel model. The lower the RMSE, the higher the fidelity of the simplified model to the complete model.

Subsequently, we employ simulation to assess the effects of parameters  $\phi$  and  $\theta$  on the accuracy of the proposed channel model. In our simulation, we traverse  $\theta$  and  $\phi$  within the ranges of  $[0^{\circ}, 90^{\circ}]$  and  $[0^{\circ}, 60^{\circ}]$  respectively, both with an interval of  $1^{\circ}$ . For each trial, we sample  $\delta_{\omega}$  from  $0^{\circ}$  to  $360^{\circ}$  at intervals of  $1^{\circ}$ , subsequently averaging RMSE across all  $\delta_{\omega}$  samples. The simulation results are presented in Fig. 5.

In Fig. 5(a), we observe that the RMSE is below 0.072 when the FOV is less than  $60^{\circ}$ . This level of error may be deemed acceptable for certain applications, such as user scheduling. Moving to Fig. 5(b), the RMSE is below 0.016 when the FOV is less than  $45^{\circ}$ , which proves suitable for applications like transmit precoding. Examining Fig. 5(c), the RMSE is below 0.0026 when the FOV is less than  $30^{\circ}$ , making it acceptable for a broad range of applications. Finally, in Fig. 5(d), the RMSE is below 0.00015 when the FOV is less than  $15^{\circ}$ , rendering this error nearly negligible.

To further illustrate the impact of the FOV on RMSE, Fig. 6 presents the curves showing the maximum and mean values of RMSE as the FOV varies. We can observe that both the RMSE and its growth rate increase with the enlargement of the FOV. When the FOV is less than  $45^{\circ}$ , the maximum value of the RMSE is below 0.016, with an average value lower than 0.0058. When the FOV is up to  $65^{\circ}$ , the average value of the RMSE is below 0.05.

Consequently, we can conclude that the loss in channel modeling accuracy due to the simplified channel model is limited, while the reduction in modeling complexity is quite significant.

#### 4.3. Applications of the simplified channel model

The simplified model can serve as a reference model for channel information extraction, significantly reducing the parameters required for obtaining channel information. When utilized for downlink channel information retrieval at the transmitter end, it reduces the overhead of feedback for uplink; When applied for user localization at the receiver end, it decreases the complexity of distance estimation equations.

The application of this model for channel information retrieval alters the computational process for obtaining channel information, necessitating adjustments to specific calculation procedures and feedback content, with minimal impact on the existing system architecture. Whether in narrow or wide FOV scenarios, the process for channel information retrieval corresponding to

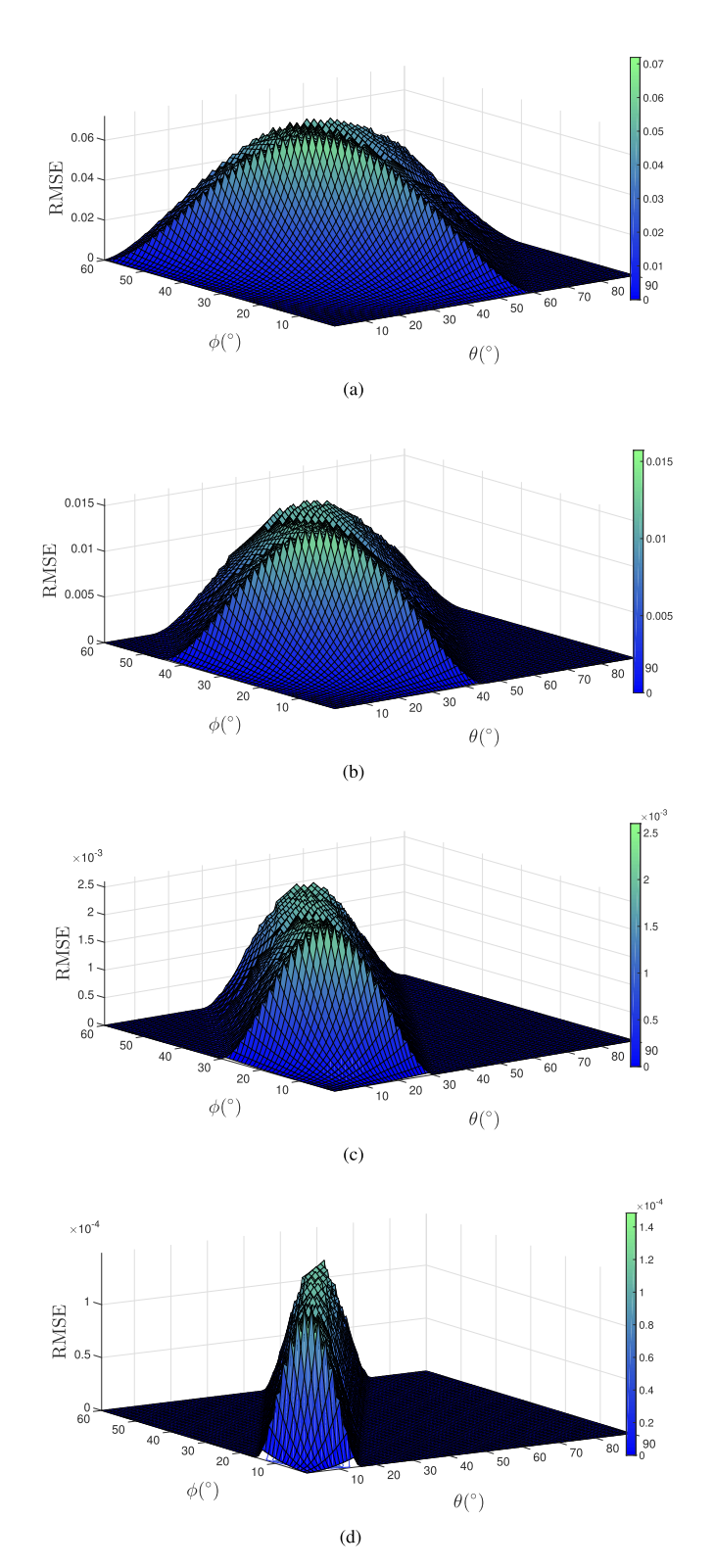


**Fig. 5.** The distribution of RMSE. (a) FOV=60°. (b) FOV=45°. (c) FOV=30°. (d) FOV=15°.

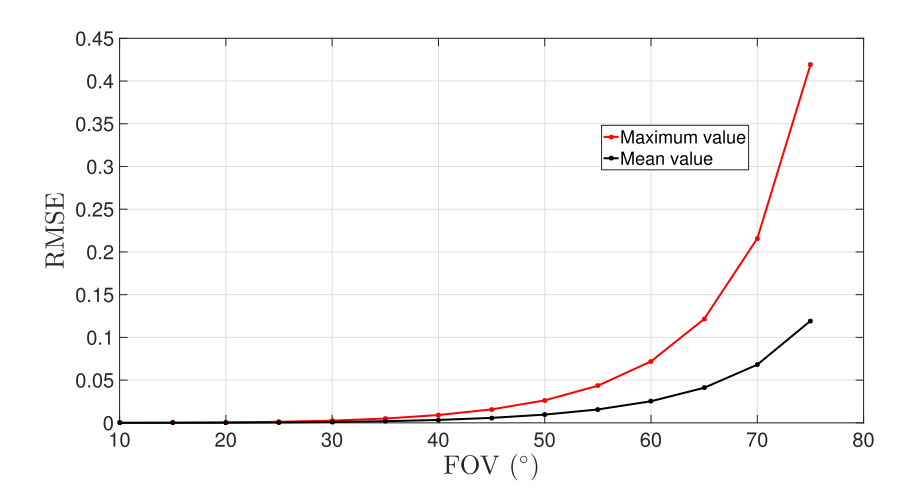


Fig. 6. The value of RMSE under different FOV settings.

this simplified model remains the same, albeit with varying degrees of accuracy in the obtained channel information.

As an illustrative example, we detail the application process of the simplified channel model through the acquisition of channel information at the transmitter. Initially, the terminal employs its onboard sensors to ascertain polarization angle data and applies positioning algorithms to secure its geographical coordinates [21]. Subsequently, this data, encompassing both the polarization angle and the terminal's position, is transmitted to the transmitter via an uplink broadcast. Armed with the stored AP coordinates and the terminal's positional data, along with the acquired polarization angle, the transmitter employs the simplified channel model to deduce the pertinent channel information.

In this simplified channel model, the azimuthal angles associated with position and orientation are substituted with predetermined values derived from the polar angles. As a result, there is no longer a necessity for the measurement of azimuthal angles, leading to a reduction in the volume of user measurement data. Moreover, this streamlined LOS channel model efficiently curtails computational complexity while maintaining an acceptable level of accuracy. It can be seen that the computational complexity of the proposed method is  $O(M(n)\log(n))$  when  $\phi + \theta \leq \Psi_c$  and  $O(M^2(n)\log^2(n))$  when  $\Psi_c < \phi + \theta < 2\pi - \Psi_c$ ,  $|\phi - \theta| < \Psi_c$ , where M(n) is the number of single precision operations required to multiply n-bit integers. The computational complexity of the current method is  $O(M^3(n)\log^3(n))$ .

#### 5. Performance evaluation of the simplified channel model

To evaluate the performance of the proposed simplified model in practical applications, this section examines its performance in the context of precoding technology, which requires a high degree of channel state information (CSI) accuracy, as a case study. We compare the performance loss when employing the simplified model versus the complete model.

In the multi-user zero forcing (ZF) precoding system, the signals are precoded using weights calculated based on a simplified channel model before they transmitted through the actual channel to the receiver. Discrepancies between the simplified channel model and the complete channel model can lead to the persistence of inter-user interference, thereby degrading user performance. In this section, we conduct a detailed analysis of the relationship between channel errors and residual interference, using a two-user precoding system as a illustrative example.

Let  $\hat{h}_m^i$  denote the channel gain between user i and access point m obtained from the proposed simplified channel model, the channel vector between user i and M access point can be represented as  $\hat{\mathbf{H}}_i = [\hat{h}_1^i, \hat{h}_2^i, \dots, \hat{h}_M^i]$ . Consequently, the ZF precoding matrix can be calculated by  $\mathbf{W} = \hat{\mathbf{H}}^H(\hat{\mathbf{H}}\hat{\mathbf{H}}^H)^{-1}$ , where  $\hat{\mathbf{H}} = [\hat{\mathbf{H}}_1^H, \hat{\mathbf{H}}_2^H]^H$ . Without loss of generality, it is assumed that the precoding weights for individual users have undergone modulus normalization. Hence, the weight vector for user i is denoted as:

$$\mathbf{W}_i = \frac{\mathbf{W}_i}{\sqrt{\mathbf{W}_i^H \mathbf{W}_i}} \tag{27}$$

For user *i*, let's denote the transmitted signal at a certain moment as  $s_i$ , and the actual channel vector between the user and M access points is  $\mathbf{H}_i = [h_1^i, h_2^i, \dots, h_M^i]$ , where  $h_m^i$  represents the actual channel gain between the user and the m-th access point. The received signal is:

$$y_i = \mathbf{H}_i \mathbf{W}_i s_i + \mathbf{H}_i \mathbf{W}_i s_i + n_i \tag{28}$$

where the first part is the desired signal, the second part is the interference signal from user j and the third part is the noise signal, which can considered as an additive Gaussian white noise with mean 0 and variance  $\sigma_i^2$ . Due to the inherent discrepancies between the channel model utilized for precoding weight computation and the complete channel model, the value of the second term no longer equals zero, which can be considered as residual interference. The residual interference is correlated with the error between the simplified channel model and the complete channel model. Assuming the signal transmission power has been normalized and using  $\Delta_i = \mathbf{H}_i - \hat{\mathbf{H}}_i$  to denote the error vector between the simplified channel model and the complete channel model, then the power of the residual interference can be expressed as:

$$I = (\mathbf{H}_i \mathbf{W}_j)^2 = ((\hat{\mathbf{H}}_i + \mathbf{\Delta}_i) \mathbf{W}_j)^2 = (\mathbf{\Delta}_i \mathbf{W}_j)^2 = |\mathbf{\Delta}_i|^2 |\mathbf{W}_j|^2 \cos^2(\beta)$$
 (29)

where  $\beta$  represents the angle between the error vector  $\Delta_{\bf i}$  and the weight vector  ${\bf W}_j$ . By substituting  $|{\bf W}_j|=1$  and  $|\Delta_{\bf i}|^2=\sum_{m=1}^M \left(h_m^i-\hat h_m^i\right)^2$  into Eq. (29), we derive the following expression:

$$I = \cos^2(\beta) \sum_{m=1}^{M} (h_m^i - \hat{h}_m^i)^2$$
 (30)

Taking into account the randomness in user location and orientation,  $\beta$  is a random variable that is uniformly distributed across the interval  $[0, \pi]$ . Therefore, we can obtain the mean of the power of the residual interference by calculating the mathematical expectation as:

$$I_{mean} = E\left[\sum_{m=1}^{M} (h_m^i - \hat{h}_m^i)^2 \cos^2(\beta)\right] = E\left[\cos^2(\beta)\right] \sum_{m=1}^{M} E\left[(h_m^i - \hat{h}_m^i)^2\right]$$
(31)

According to RMSE definition provided by Eq. (26), we can approximate the following expression:

$$E[(h_m^i - \hat{h}_m^i)^2] \approx RMSE \sum_{m=1}^M E[(h_m^i)^2]$$
 (32)

Since  $\beta$  is a random variable uniformly distributed across the interval  $[0, \pi]$ , we can get  $E[\cos^2(\beta)] = 1/2$ . Substituting  $E(\cos^2(\beta)) = 1/2$  and Eq. (32) into Eq. (31), we can get:

$$I_{mean} \approx \frac{1}{2} RMSE \sum_{m=1}^{M} E[(h_m^i)^2]$$
(33)

The Eq. (33) reveals that residual interference depends on both channel errors and the channel gain. The impact of residual interference on user rate can be characterized by the

signal-to-interference ratio (SIR):

$$SIR \approx 10 \lg \frac{\sum_{m=1}^{M} E[(\hat{h}_{m}^{i})^{2}]}{\frac{1}{2}RMSE\sum_{m=1}^{M} E[(\hat{h}_{m}^{i})^{2}]} = 10 \lg \frac{2}{RMSE}$$
 (34)

Referring to the data of the mean value of *RMSE* for different FOV settings presented in Fig 6, we can approximate the corresponding mean SIR for various FOVs in Fig 7.

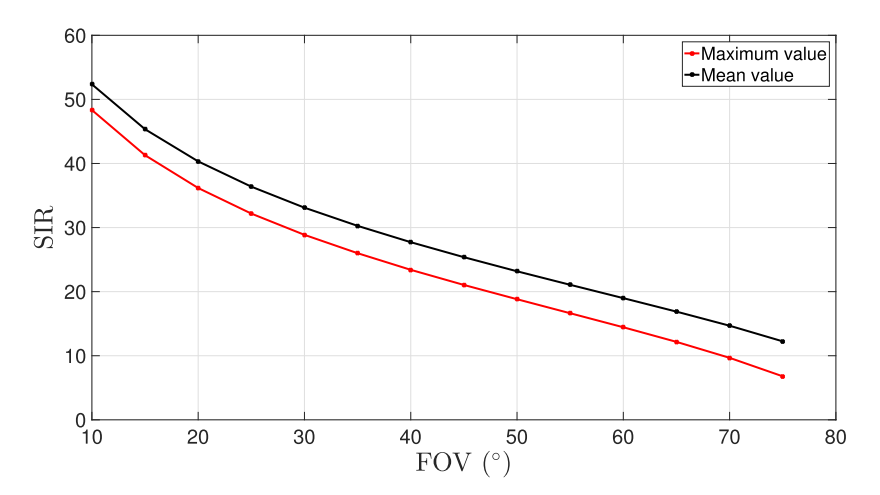


**Fig. 7.** The SIR under different FOV settings.

Figure 7 depicts a decline in the SIR with an increasing FOV. When the FOV does not exceed 45° degrees, the average and maximum values of the SIR are both above 20 dB. However, when the FOV exceeds 60°, the average and maximum values of the SIR are both below 20 dB. The impact of SIR on user rate is also related to the signal-to-noise ratio (SNR). When the SIR is lower than the SNR, the interference power exceeds the noise power, and the residual interference significantly affects the user rate. Conversely, when the SIR is higher, the residual interference has a less noticeable impact on the user rate. To specifically assess the impact of residual interference on user rate under different SNR conditions, we introduce the rate loss as a metric for evaluation as:

$$Loss = \frac{r - \hat{r}}{r} \tag{35}$$

where r and  $\hat{r}$  represent the user rates corresponding to the precoding schemes based on the complete channel model and the simplified channel model, respectively. Due to the high SNR characteristic of indoor VLC systems, we use the reachability ratio proposed in [22] to approximate the user rate:

$$r_i = \frac{1}{2}\log_2(1 + \omega \gamma_i) \tag{36}$$

where  $\omega = \frac{e}{2\pi}$  (e = 2.71 is the Euler number). Referring to the data of the SIR for different FOV settings presented in Fig 7, Fig 8 presents the user rate loss curves corresponding to various SNRs at different given FOVs.

As observed in Fig 8, for a fixed FOV, the average and maximum values of the user rate loss due to residual interference both increase with an increase in the SNR. When the SNR is below 20 dB, users with an FOV not exceeding  $40^{\circ}$  degrees experience a mean rate loss not exceeding 2% and a maximum rate loss not exceeding 4.5%. However, for FOV surpassing  $50^{\circ}$ , the user rate loss escalates sharply. At an FOV of  $60^{\circ}$ , the mean rate loss is 11.5% and the maximum

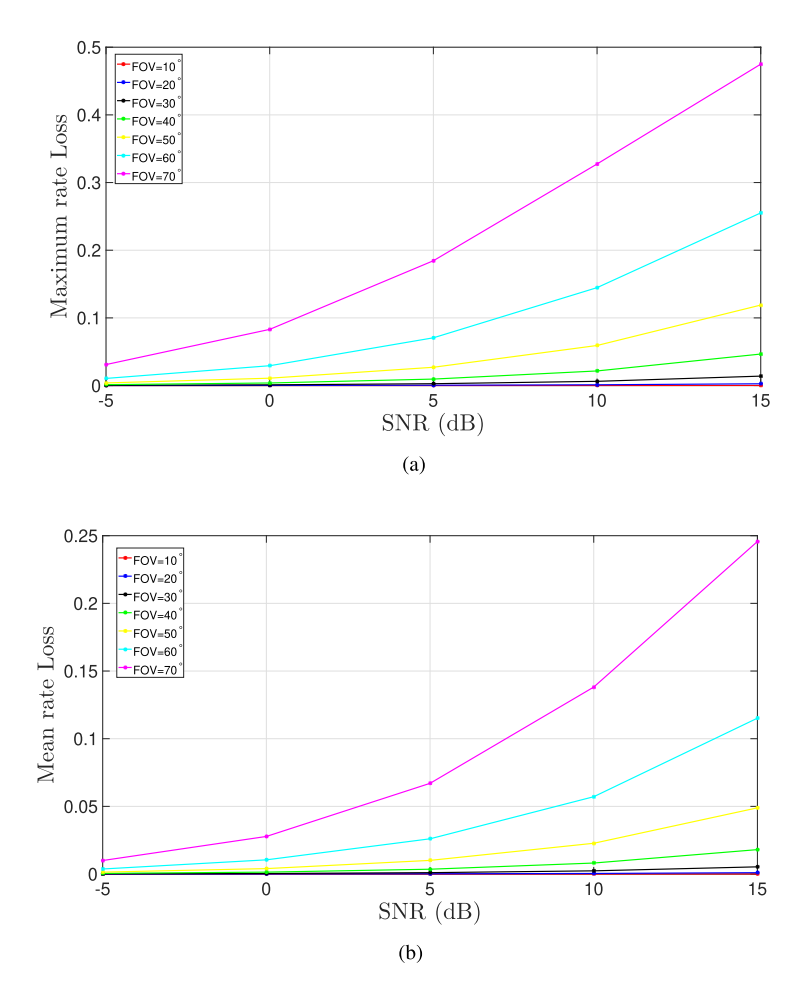


**Fig. 8.** The loss of user rate under different FOV settings. (a) Maximum loss. (b) Mean loss.

rate loss is 26%, and they further ascends to 24.5% and 48% at a 70° FOV. Simulation results validate that, at a given SNR, wider FOVs are correlated with increased residual interference, consequently resulting in higher user rate loss. Furthermore, in order to provide a comprehensive assessment of user rate loss, Fig 9 illustrates the variation of the average and maximum values of the user rate loss under different FOV settings with SNR=5dB.

From Fig 9, it can be observed that when the FOV is less than  $45^{\circ}$ , both the maximum rate loss and the average rate loss do not exceed 1%. However, when the FOV exceeds  $45^{\circ}$ , the user rate loss increases sharply, with the maximum rate loss showing a faster rate of increase.

The performance analysis of a two-user precoding system based on a simplified channel model indicates that, when the FOV does not exceed 45°, the performance degradation caused by residual interference resulting from the simplified channel model is limited. Despite this, the simplified channel model significantly reduces the required number of parameters for channel modeling, thereby effectively reducing the overhead associated with CSI feedback. Consequently, its application in specific scenarios holds considerable significance.

For applications such as precoding, which require high accuracy in CSI, the proposed simplified channel model still demonstrates satisfactory performance in scenarios with narrow-FOV. Additionally, this simplified channel model can be extended to applications in wide-FOV

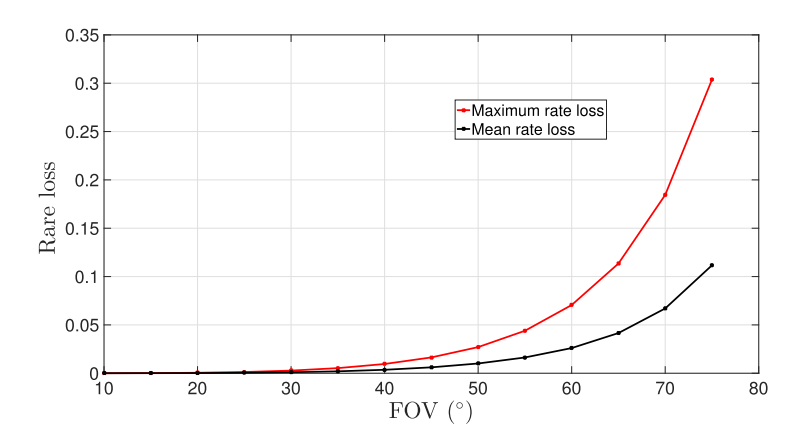


Fig. 9. The rate loss under different FOV settings with SNR=5dB.

networks with lower requirements for channel accuracy, such as user scheduling and resource allocation, thereby broadening the applicability of the simplified model. The specific application and performance analysis of the proposed simplified channel model in a diverse range of scenarios is among the key areas of our future research.

#### 6. Conclusion

In this paper, we derive the analytical expression for the LOS channel gain concerning the user terminal device's position and orientation. A quantitative analysis of the azimuthal angle's impact on indoor VLC channels reveals its limited effect, particularly in scenarios with a narrow FOV. Additionally, we identify a convenient substitute for the azimuth angle that minimally influences the LOS channel model's estimation accuracy. Leveraging these insights, we propose a simplified LOS channel model tailored for indoor VLC systems. Employing the RMSE as a performance metric, we evaluate the modeling loss incurred by employing the proposed simplified channel model in comparison to a complete channel model. The evaluation results reveal that the receiver's FOV plays a pivotal role in the accuracy of the simplified channel modeling, where narrow FOVs result in a reduced modeling loss. Moreover, we conduct an analysis of the user rate loss introduced by the simplified model for a two-user precoding indoor VLC system, providing insights into its practical application. Based on the research results, we recommend the application of the proposed channel model for narrow-FOV systems that require high channel accuracy. Additionally, this simplified channel model is suitable for wide-FOV systems where the CSI does not need to be highly precise. The implementation of the proposed simplified channel model would involve incorporating corresponding computational processes and feedback content without requiring major hardware or communication protocol changes.

However, it's imperative to note that the proposed mode only simplifies LOS channel modeling, neglecting non line-of-sight (NLOS) components. In our next research phase, we plan to investigate whether the principles underlying the simplified model can be extended to NLOS channel modeling. Moreover, we intend to further evaluate the performance of the simplified channel model in various applications such as user scheduling and indoor positioning. Based on these evaluations, we will refine the model accordingly to broaden its applicability. We anticipate that our findings will inspire further exploration into the optimization of VLC systems, particularly in scenarios where balancing model complexity and CSI accuracy is crucial.

Funding. National Natural Science Foundation of China (62101444, 62271091).

**Disclosures.** The authors declare no conflicts of interest.

**Data availability.** Data underlying the results presented in this paper are not publicly available at this time but may be obtained from the authors upon reasonable request.

#### References

- H. Yang, W.-D. Zhong, C. Chen, et al., "Coordinated resource allocation-based integrated visible light communication and positioning systems for indoor IoT," IEEE Trans. Wireless Commun. 19(7), 4671–4684 (2020).
- S. Ma, R. Yang, B. Li, et al., "Optimal power allocation for integrated visible light positioning and communication system with a single LED lamp," IEEE Trans. Commun. 70(10), 6734–6747 (2022).
- 3. S. P. Dash, "Performance analysis for a narrow-FoV VLC system with random user orientation," in 2023 International Conference on Microwave, Optical, and Communication Engineering (ICMOCE), (2023), pp. 1–4.
- X. You, Y. Zhong, J. Chen, et al., "Mobile channel estimation based on decision feedback in vehicle-to-infrastructure visible light communication systems," Opt. Commun. 462, 125261 (2020).
- F. Miramirkhani and M. Uysal, "Channel modeling and characterization for visible light communications," IEEE Photonics J. 7(6), 1–16 (2015).
- X. Nan, P. Wang, L. Guo, et al., "A novel VLC channel model based on beam steering considering the impact of obstacle," IEEE Commun. Lett. 23(6), 1003–1007 (2019).
- C. Chen, X. Zhong, S. Fu, et al., "OFDM-based generalized optical MIMO," J. Lightwave Technol. 39(19), 6063–6075 (2021).
- 8. J. Kahn and J. Barry, "Wireless infrared communications," Proc. IEEE 85(2), 265-298 (1997).
- T. Komine and M. Nakagawa, "Fundamental analysis for visible-light communication system using LED lights," IEEE Trans. Consumer Electron. 50(1), 100–107 (2004).
- W. Xu, J. Wang, H. Shen, et al., "Indoor positioning for multiphotodiode device using visible-light communications," IEEE Photonics J. 8(1), 1–11 (2016).
- 11. Y. S. Eroglu, Y. Yapici, and I. Guvenc, "Impact of random receiver orientation on visible light communications channel," IEEE Trans. Commun. **67**(2), 1313–1325 (2019).
- 12. M. D. Soltani, A. A. Purwita, Z. Zeng, *et al.*, "Modeling the random orientation of mobile devices: measurement, analysis and LiFi use case," IEEE Trans. Commun. **67**(3), 2157–2172 (2019).
- 13. J. Chen, I. Tavakkolnia, C. Chen, *et al.*, "The movement-rotation (MR) correlation function and coherence distance of VLC channels," J. Lightwave Technol. **38**(24), 6759–6770 (2020).
- X. Zhu, C.-X. Wang, J. Huang, et al., "A novel 3D non-stationary channel model for 6G indoor visible light communication systems," IEEE Trans. Wireless Commun. 21(10), 8292–8307 (2022).
- R. K. Pal, S. P. Dash, S. Joshi, et al., "Channel estimation and performance analysis of a wide-FOV visible light communication system with random receiver orientation and location," IEEE Trans. Wireless Commun. 22(3), 1964–1979 (2023).
- S. Zhang, P. Du, H. Yang, et al., "Recent progress in visible light positioning and communication systems," IEICE Trans. Commun. E106.B(2), 84–100 (2023).
- C. Le Bas, S. Sahuguede, A. Julien-Vergonjanne, et al., "Impact of receiver orientation and position on visible light communication link performance," in 2015 4th International Workshop on Optical Wireless Communications (IWOW), (2015), pp. 1–5.
- M. Dehghani Soltani, A. A. Purwita, I. Tavakkolnia, et al., "Impact of device orientation on error performance of LiFi systems," IEEE Access 7, 41690–41701 (2019).
- S. Shen, S. Li, and H. Steendam, "Hybrid position and orientation estimation for visible light systems in the presence of prior information on the orientation," IEEE Trans. Wireless Commun. 21(8), 6271–6284 (2022).
- S. Ma, J. Wang, C. Du, et al., "Joint beamforming and PD orientation design for mobile visible light communications," IEEE Trans. Wireless Commun. 22(8), 5056–5069 (2023).
- S. Liu, X. Wang, J. Song, et al., "Cooperative robotics visible light positioning: an intelligent compressed sensing and GAN-enabled framework," IEEE Journal of Selected Topics in Signal Processing (2024).
- A. Lapidoth, S. M. Moser, and M. A. Wigger, "On the capacity of free-space optical intensity channels," IEEE Trans. Inf. Theory 55(10), 4449–4461 (2009).